







Visualization of defects in single-crystal and thin-film PdCoO₂ using aberration-corrected scanning transmission electron microscopy

Celesta S. Chang ^{1,2,*},[†] Jiaxin Sun ³ Seunghyun Khim ⁴ Andrew P. Mackenzie ^{4,5}
Darrell G. Schlom ^{3,6} and David A. Muller ^{2,6}

¹*Department of Physics, Cornell University, Ithaca, New York 14853, USA*

²*School of Applied and Engineering Physics, Cornell University, Ithaca, New York 14853, USA*

³*Department of Materials Sciences and Engineering, Cornell University, Ithaca, New York 14853, USA*

⁴*Max Planck Institute for Chemical Physics of Solids, Nöthnitzer Straße 40, 01187 Dresden, Germany*

⁵*SUPA, School of Physics and Astronomy, University of St. Andrews, St. Andrews KY16 9SS, United Kingdom*

⁶*Kavli Institute at Cornell for Nanoscale Science, Cornell University, Ithaca, New York 14853, USA*



(Received 6 February 2022; revised 21 June 2022; accepted 19 August 2022; published 2 September 2022)

Single-crystal delafossite PdCoO₂ is known to have an extremely low intrinsic impurity concentration of $\sim 0.001\%$, demonstrating extraordinarily high conductivity with a mean free path of $\sim 20 \mu\text{m}$ at low temperatures. However, when grown as thin films, the resistivity at room temperature increases by a factor of 3–80 times, depending on the film thickness. Using scanning transmission electron microscopy, we identify different classes of defects for the single crystal vs epitaxial thin film. The dominant defect for single-crystal PdCoO₂ is found to be ribbonlike defects. For the thin films, we identify different types of defects arising in epitaxial thin films mainly due to substrate termination that disrupt the lateral connectivity of the conducting planes. Our results are consistent with the high conductivity of single crystals and increased electrical resistivity of the thin films compared to that of single crystals, suggesting that selecting a proper substrate, improving surface quality, and reducing the step density are the keys to enhance the film quality for utilizing PdCoO₂ as a platform for future applications.

DOI: [10.1103/PhysRevMaterials.6.093401](https://doi.org/10.1103/PhysRevMaterials.6.093401)

I. INTRODUCTION

Bulk delafossite PdCoO₂ is known for its remarkable in-plane resistivity as low as 8 nΩ cm with mean free paths as long as 20 μm at low temperatures [1]. Recently, Sunko *et al.* reported that such high conductivity is a result of extraordinary intrinsic purity of the materials with point defect concentrations as low as 0.001% [2]. Owing to its high conductivity, the potential of PdCoO₂ and other metallic delafossites [3] as a platform for studying quantum transport [4,5] as a component of spintronic devices [6] or as thermoelectric devices [7,8] has been of great interest. Nevertheless, the quality of epitaxial thin films, which is vital to device applications, is still at an early stage. In 2018, Harada *et al.* first reported the epitaxial growth of ultrathin PdCoO₂ films on *c*-plane Al₂O₃ by pulsed-laser deposition [9]. Shortly thereafter, the growth of PdCoO₂ thin films on *c*-plane Al₂O₃ using molecular-beam epitaxy (MBE) was reported [10,11]. The advantages of thin PdCoO₂ films are demonstrated by the recent successful control of Schottky barrier heights using

the interface dipole effect of the inserted PdCoO₂ layer in metal/ β -Ga₂O₃ junctions [12].

Compared to single crystals, PdCoO₂ thin films grown on Al₂O₃ tend to show much higher in-plane resistivities, which increase as the film thickness decreases [9–11]. This is expected for a thin film as it experiences limitations, such as boundary conditions imposed at its interfaces and grain boundaries that could act as scattering centers [9,10]. From the growth perspective, whereas bulk-growth processes occur near thermodynamic equilibrium conditions, thin-film growth techniques are generally carried out further from equilibrium conditions. This results in the growth process being dominated by the diffusive kinetics of adatoms on the growth surfaces. As a result, thin films can easily deviate from stoichiometry, resulting in various point defects inside the film [13,14]. The conduction of PdCoO₂ is dominated by Pd two-dimensional (2D) layers as CoO₂ layers are insulating [15,16]. Thus, resistivity in bulk PdCoO₂ is expected to be dominated by defects on the conductive Pd planes. In particular, defects that disrupt continuity of the Pd planes could have detrimental effects on the electrical properties. Controlling such defects are, therefore, crucial to improve film properties towards bulk-like perfection, which can be achieved by first understanding the defect types that occur in this system at the atomic scale.

In this paper, we report the first atomic-resolution images of defects in PdCoO₂ both for as-grown bulk PdCoO₂

*Corresponding author: celesta@mit.edu

[†]Present address: Research Laboratory of Electronics, Massachusetts Institute of Technology, Cambridge, Massachusetts 02139.

and for an 8-nm-thick film of PdCoO₂ grown on *c*-plane Al₂O₃ by MBE, using aberration corrected scanning transmission electron microscopy (STEM). The transport properties of this thin film were measured, and the room-temperature resistivity and residual resistivity ratio (RRR) were found to be degraded with respect to the single crystal [10]. With medium-angle annular dark field (MAADF-STEM) imaging of single-crystal PdCoO₂, we observe ribbonlike defects ranging a few hundred nanometers in lateral length that are likely dislocations or stacking faults. High-angle annular dark field (HAADF-) and annular bright field (ABF-STEM) imaging of thin film PdCoO₂ reveals 180° in-plane rotation twin domains created by the energetic equivalence of nucleating such PdCoO₂ domains on the (001) surface of the Al₂O₃ substrate. Meanwhile, we report that majority of defects-, such as out-of-phase boundaries, Pd-rich agglomerates, and unambiguous twin domains which we report in this paper—are induced by the substrate surface termination, which is correlated with these PdCoO₂ thin films having inferior electrical characteristics compared to single crystals. The quality of PdCoO₂ film growth dependence on the substrate surface quality can be a limiting factor for future applications, which would require specific strategies for improvement.

II. METHODS

Single crystals of PdCoO₂ were grown in sealed quartz tubes as described in Ref. [2]. The as-grown crystals had platelet forms and were 3–8 μm in thickness and 300–700 μm in lateral dimensions. A thin film of PdCoO₂ with a thickness of 8 nm was grown on *c*-plane sapphire at 480 °C (measured by a thermocouple in the vicinity of the substrate but not in thermal contact with it) under a background partial pressure of 10⁻⁵ Torr of distilled ozone (80% O₃ + 20%O₂) in a Veeco Gen10 MBE system. Al₂O₃ substrates (CrysTec GmbH) with (001)-orientation and a miscut angle of ±0.1° are annealed in air at 1050 °C for 6 h prior to growths to yield a step-and-terrace morphology. More information on detailed growth conditions, surface characterization, and electrical transport results for the thin films can be found in Ref. [10].

Cross-sectional [210], plan-view TEM specimens of single-crystal and cross-sectional [100] TEM specimens of thin film PdCoO₂ were prepared using a FEI Strata 400 focused ion beam (FIB) where a PdCoO₂ lamella with a typical volume of ~20(width) × 5(height) × 2(thickness) μm³ was extracted and thinned down to ~18 × 5 × 0.05 μm³ by Thermo Fisher Helios G4 UX FIB with a final milling step of 5 keV to reduce damage. Carbon and platinum layers were sputtered on the sample surface prior to FIB thinning to minimize potential damage from ion milling. The samples were then examined by STEM, using an aberration-corrected Titan Themis operating at 300 keV for atomic-resolution imaging and also a Tecnai F20 at 200 keV for wide-field surveys. A convergence angle of 21 mrad was used on the Titan and 9 mrad on the Tecnai. HAADF-STEM imaging was performed with an inner cutoff angle of 40 mrad, whereas MAADF-STEM imaging was

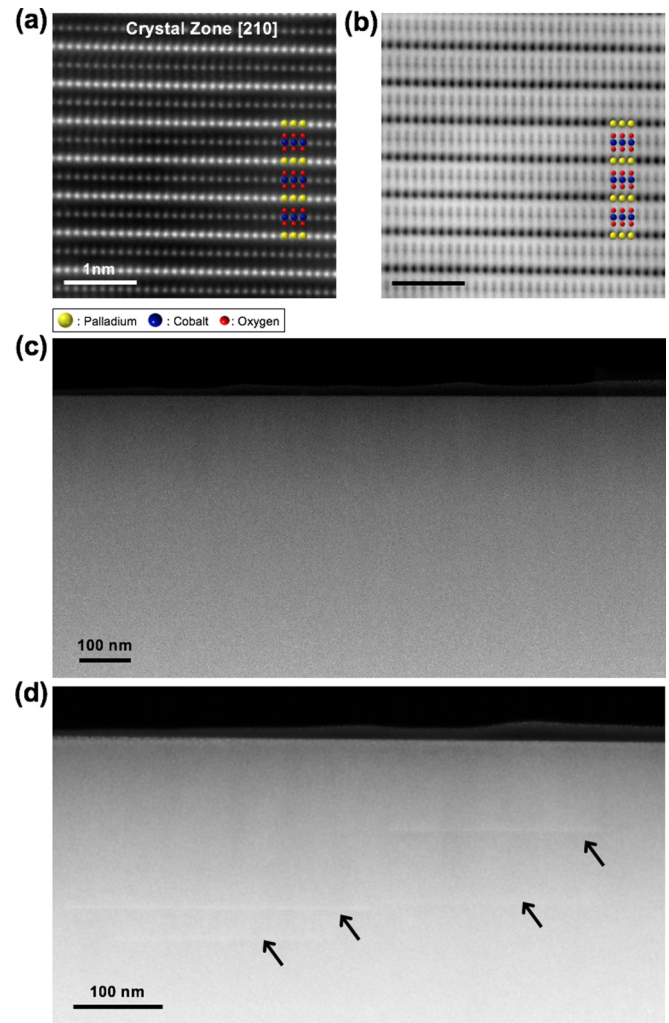


FIG. 1. STEM images of single-crystal PdCoO₂. (a) HAADF-STEM image of pristine PdCoO₂ imaged along the [210] zone axis resolving Pd and Co atomic sites. (b) Simultaneously taken ABF-STEM image of PdCoO₂ resolving Pd, Co, and O. Overlaid yellow, blue, and red spheres in the crystal structure correspond to Pd, Co, and O, respectively. (c) Image of a pristine region taken at low magnification. (d) Defects in pure PdCoO₂ are captured by MAADF-STEM imaging.

performed with an inner cutoff angle of around 30 mrad in Tecnai F20 to obtain strain-sensitive images.

III. RESULTS AND DISCUSSIONS

A. Defects in Pure Single Crystals

Using STEM, we investigated single crystals of PdCoO₂, looking at a total volume of 36 μm³ by preparing six cross-sectional TEM samples and two plan-view TEM samples extracted from four different crystals. Figures 1(a) and 1(b) show simultaneously acquired atomic resolution HAADF-STEM and ABF-STEM cross-sectional images, respectively. Pd and Co sites are resolved in Fig. 1(a), whereas the ABF signal of Fig. 1(b) resolves the oxygen atoms as well. Typical TEM samples prepared by FIB have a thickness ranging from 20–50 nm, which is along the direction that we see in

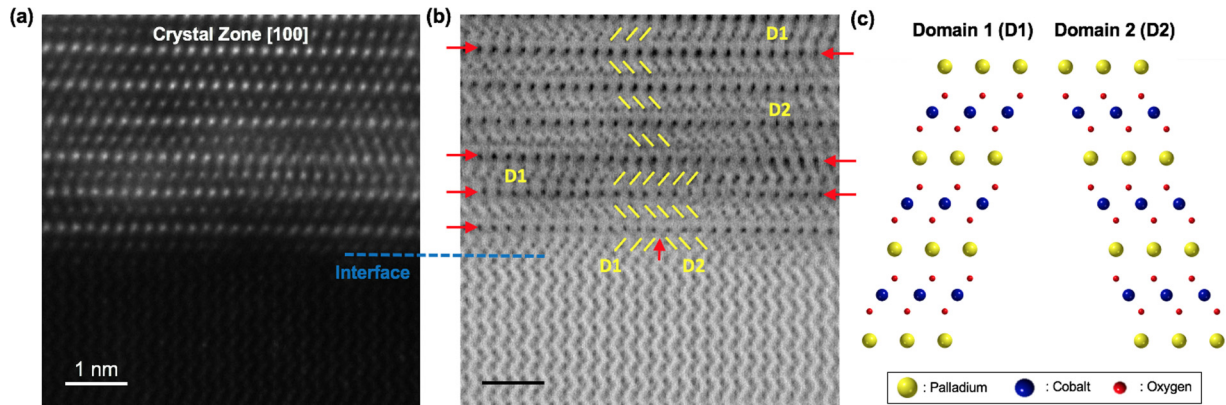


FIG. 2. Formation of twin domains in PdCoO₂ at the interface and inside the film. (a) HAADF-STEM image along the [100] zone axis. (b) Simultaneously acquired ABF-STEM image reveals the CoO₂ layer that has different bonding directionalities, revealing the location of two different twin domains denoted as domain 1 (D1) and domain 2 (D2). Twin boundaries are distinguished by red arrows. A raw ABF-STEM image is provided in Ref. [17]. (c) Crystal schematics for two different twin domains D1 and D2, related by a 180° in-plane rotation from each other.

projection. Thus, the atomic contrast we get is an average over ~50–150 atoms along each resolved column. Compared to 2D monolayers, such as MoS₂ or graphene, detection of a single vacancy or an interstitial, therefore, becomes more difficult as it is only ~1/100 atoms here, comparable to our detection limits (See Fig. S1 in the Supplemental Material for more details [17]). The electron beam also experiences channeling as it propagates along the column, so the same number of point defects can yield different intensities depending on the location they occupy along the column [18]. As we were not able to observe any measurable contrast differences from point defects in the images, we believe the concentration of isolated point defects—vacancies or interstitials—are less than the detection limit of HAADF-STEM (~1%/atom column). Much thinner samples would be needed for single atom sensitivity at which point vacancies could be detected and counted, and a more useful upper bound could be placed.

In most samples from the single crystal, we were able to observe pristine areas ranging from several microns in lateral dimensions as in Fig. 1(c). To obtain enhanced contrast from strained areas, MAADF-STEM imaging was used in Fig. 1(d), revealing regions with thin long defects extending about 200–300 nm in the lateral dimension but only about 2 nm wide. The contrast from these defects tend to disappear during STEM observation even with small sample tilts, indicating that the depths of the defect should be at the scale of a few nanometers. The density of these defects are approximately calculated to be slightly less than 0.001% in volume, in good agreement with Ref. [2]. These defects only appear as strain fields in low magnification TEM images without any visible change in lattice structure. When magnified, the lattice structure is not so different from the bulk structure of Fig. 1(a). This is related to the fact that we are observing a projection of 20–50 nm in thickness where the atomic arrangements of an embedded defect can be obscured if the defects are very thin. As plan-view [001] TEM imaging of the specimen also showed similar results, we suspect that the defects are likely to be very thin ribbonlike defects, such as dislocations or stacking faults. Since we were not able to see much change in the lattice

structure by HAADF-STEM imaging, understanding its formation mechanism by detailed careful observation of the atomic arrangements should be performed in the future—perhaps by scanning electron-beam nanodiffraction which is capable of capturing small local changes in atomic arrangements without beam damage.

B. Defects in Thin-Film PdCoO₂

Whereas the room-temperature in-plane resistivity of single-crystal PdCoO₂ is 2.6 μΩ cm when grown as thin films with varying thicknesses from 10 nm down to 3 unit cells (1.6 nm), the resistivity at room temperature increases by a factor of 3 to 80 times, respectively, with the resistivity reaching a plateau with increasing film thickness [10]. The resistivity of our 8-nm-thick film of PdCoO₂ which we will discuss later in this paper, is 11 μΩ cm at room temperature [10]. Furthermore, the RRR which is as high as 347 for single crystals, was significantly reduced to 2 for the 8-nm-thick film. The increase in resistivity is a common feature for thin films of metallic oxides due to confinements imposed by the thin-film geometry, reducing the mean free path of conduction electrons by increased surface scattering effects [19,20]. However, in light of the high defect density of these films (described below), it would be necessary to understand the types of defects.

The (001)-oriented epitaxial growth of PdCoO₂ on (001) Al₂O₃ follows from its lattice match (−2.9% when the crystal structures are rotated in plane by 30° with respect to each other), trigonal crystal symmetry, and the chemically isomorphic CoO₂ surface termination of PdCoO₂ [9,10]. PdCoO₂ films grow with the expected 30° in-plane rotation to the underlying substrate, but it is energetically equivalent for both a +30° rotation angle and a −30° rotation angle. The result is that both ±30° nuclei form and in doing so, the film consists of two nonequivalent twin domains related by an in-plane rotation of 180° [9,10]. Figure 2 shows an example of rotational twinning at the interface of PdCoO₂ and Al₂O₃. The HAADF-STEM image in Fig. 2(a) shows heavy Pd and Co atomic layers. The simultaneously acquired ABF-STEM

image in Fig. 2(b) gives less contrast between both heavy and light atoms, making it possible to simultaneously detect the oxygen atoms, resolving the CoO_2 layer and, therefore, the O-Co-O bonding directionality (See Fig. S2 in the Supplemental Material [17] for raw ABF-STEM image without overlaid graphics). At the interface we observe two distinct twin domains with 180° rotated bonding directions as highlighted by the yellow lines overlaid on O-Co-O bonds (two regions where the film structure is 30° and -30° rotated from the substrate). These two twin domains, namely, D1 and D2 are specified by the crystal schematics in Fig. 2(c). The twin domain structures are shown to alternate between D1 and D2 along the growth direction. Also, twin boundaries are not perpendicular to the interface, but rather switch continuously at different locations at each in-plane CoO_2 layer creating meandering twin boundaries which we discuss later in this paper.

As discussed in Refs. [10,21], the lattice mismatch between Al_2O_3 and PdCoO_2 along the (001) direction can lead to the formation of out-of-phase boundaries (OPBs) [22] as the palladium planes can be out of registry depending on where the CoO_2 layer starts to nucleate on the sapphire substrate. In Fig. 3(a), abrupt termination of a Pd layer is caused by surface steps at the interface. Although the Pd/ CoO_2 layers grown above are not highly affected, in (b) they have formed a broad OPB but still maintain partially intact conductive Pd layers. Figure 3(c) shows OPBs caused by the surface steps that resulted in disruption of the Pd layer, which could be more detrimental to the electrical properties than the previous two cases.

Point defects can also affect the electrical properties especially when they disrupt the continuity of conductive Pd layers. The most energetically stable Pd interstitial position for PdCoO_2 is calculated to be when a Pd atom is positioned to bond to two oxygen atoms above and two Pd atoms below or vice versa (see Fig. S3 in the Supplemental Material [17]) [2]. Although we were not able to observe a single interstitial located at this position, a similar configuration was observed in Fig. 4 where we can see multiple Pds viewed in projection, located at the interstitial position, collected into a line defect (e.g., such as one might expect at a dislocation core [23]). On average these were observed with a spacing of roughly once every 220 nm (± 7 nm). With the aid of ABF imaging, we observe that these agglomerates tend to occur at the twin boundaries along with surface steps as shown in Fig. 4(a). The atomic step of the interface is outlined by a white line (raw image available in Fig. S4 of the Supplemental Material [17]). Here, we can see that these agglomerates are located on top of the atomic step where a twin boundary also occurs. Atomic steps may be low-energy nucleation locations for twin boundaries as well as for Pd interstitials. The different O-Co-O bond directionality for the two twin domains that meet at the twin boundary creates a wider gap between the neighboring Pd atoms. This allows a much wider space available for an interstitial to be positioned, which would also lower the overall formation energy. The schematics are presented in Fig. S4 of the Supplemental Material [17]. Local nonstoichiometry, which results from relatively low growth temperature with limited adatom mobilities, can also aid formation of such interstitials. The regions boxed in blue in the HAADF-STEM

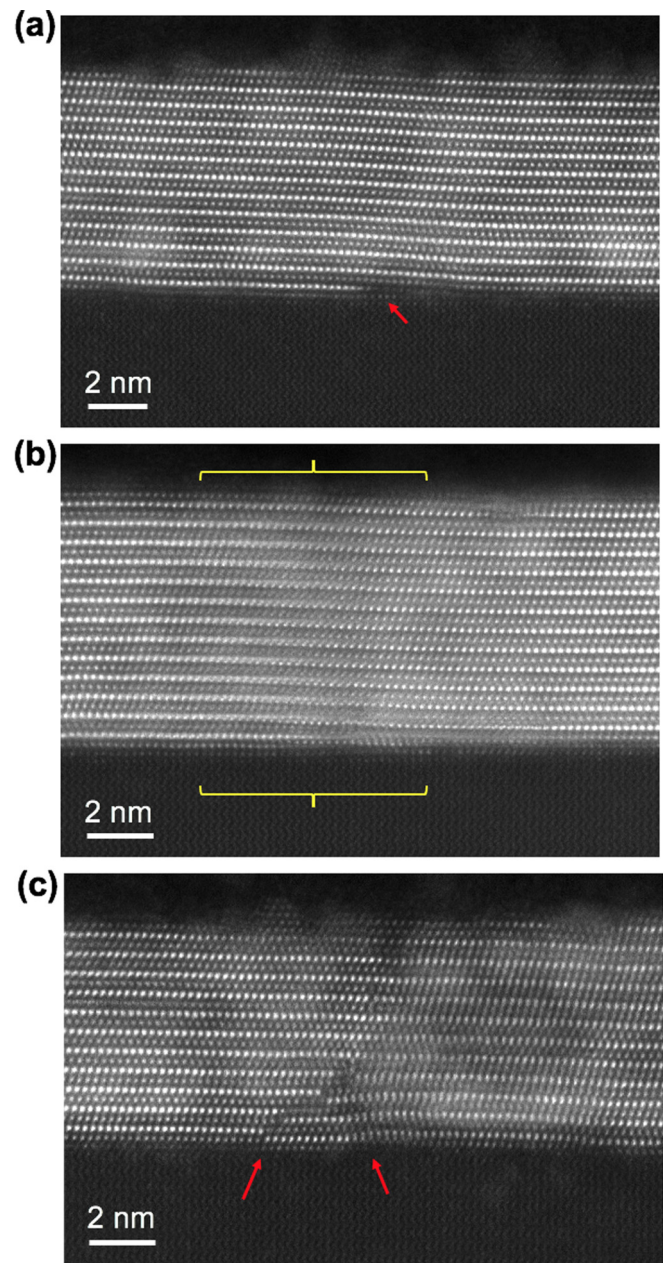


FIG. 3. Stacking defects in PdCoO_2 films. (a) Termination of one Pd layer by a step edge in the substrate. (b) Out-of-phase boundaries (in yellow brackets) are formed from the step edge at the interface, but the Pd layers remain partially connected. (c) Large lattice mismatch along the c axis from atomic steps at the interface can result in the formation of OPBs with disconnected Pd layers (red arrows).

image shows a shorter Co-Co distance compared to other regions. This is due to the overlap of twin domains D1 and D2. As a result, in the ABF-STEM image we can observe a discrete zigzag structure of the overlapped CoO_2 structure. Figure 4(b) shows a similar case where the agglomerates has formed on top of an atomic step at the interface. These Pd-rich agglomerates also occur frequently far away from the interface as shown in Fig. 4(c), which is formed along the twin boundaries. Here, we can see meandering twin boundaries as the twin domains switch continuously at different locations

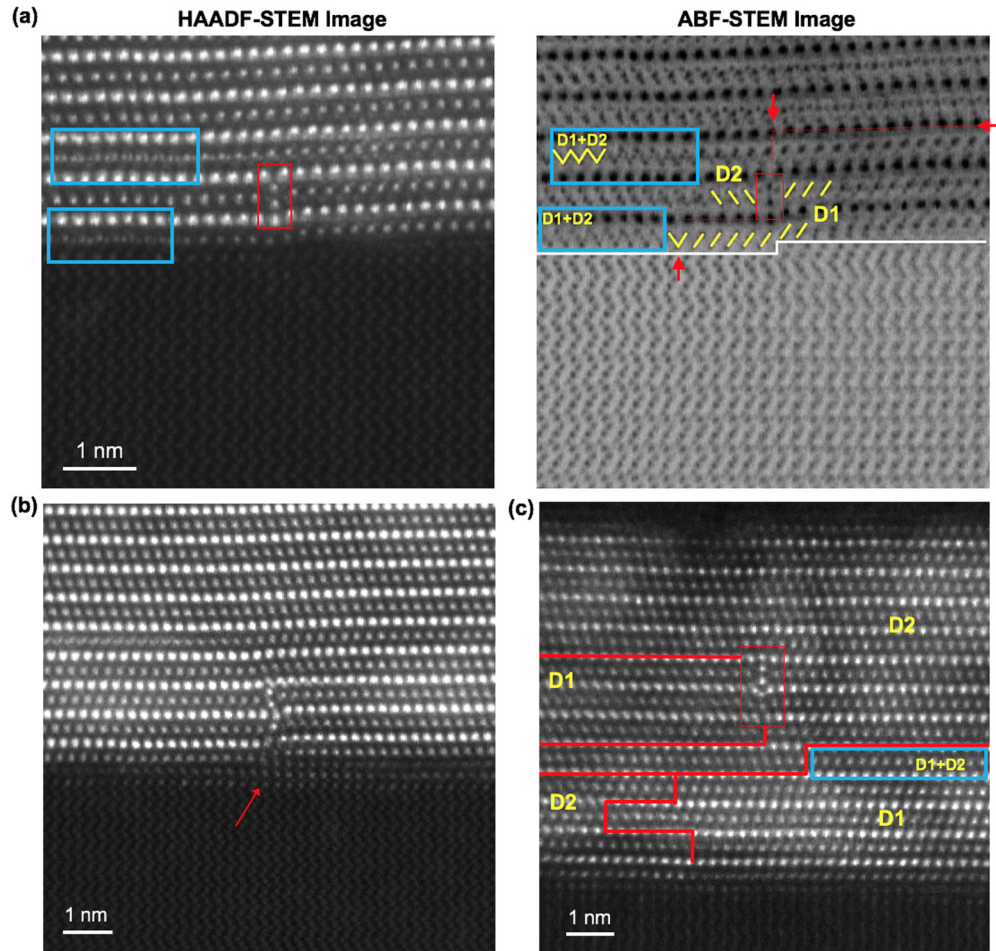


FIG. 4. Pd agglomerates formed along the growth direction. ABF-STEM image in (a) shows the twin domain boundary (along the red lines) outlined by comparing the CoO_2 bonding directionality. Twin domain variants are labeled as D1 or D2. Agglomerates are frequently observed near twin boundaries as shown inside the red boxed region in (a). Red arrows show the domain boundaries. Raw ABF-STEM image is provided in Ref. [17]. The boxed region in blue shows an overlapped lattice structure of domains D1 and D2 along the beam direction. (b) shows agglomerates formed along the atomic step at the interface (red arrow). (c) shows agglomerates formed along the twin boundaries (inside the boxed region in red) without atomic steps or dislocations at the interface.

in each CoO_2 layer. Since these agglomerates are formed perpendicular to the Pd conductive planes, these would appreciably contribute to the increase in resistivity.

Our observations indicate that in order to improve the film properties, we would need a suitable buffer layer to mitigate defects and use other trigonal substrates with better lattice mismatch to relieve and eliminate the twinning. This has been recently discussed by Ok and co-workers where they have seen higher quality growths of PdCrO_2 when grown on a monolayer-thick CuCrO_2 buffer layer [24,25]. However, the CuCrO_2 buffer layer was found to form $\text{CuCr}_{1-x}\text{Al}_x\text{O}_2$ delafossite at the $\text{CuCrO}_2/\text{Al}_2\text{O}_3$ inducing homogenous and stable nucleation with delafossite symmetry where this preferential nucleation by Al substitution only occurs for Cu-based delafossites [25]. Therefore, more research is needed to find an optimal buffer layer for Pd-based delafossites. Extending the delafossite buffer layer concept further, the ideal substrate for the growth of delafossite films is likely to be a chemically and structurally compatible delafossite single crystal. Single crystals of the delafossite CuFeO_2 with a diameter of 10 mm

and several centimeters in length were recently produced [26]. This size is sufficient to be used as substrates for the growth of thin films.

The formation of OPBs and frequent Pd agglomerates due to surface steps suggests that the growth of PdCoO_2 benefits from perfectly flat substrate surface, or more ideally, a substrate with controllable surface termination to obtain high quality thin films [10,21]. Another recent study reported the growth of a single domain CuCrO_2 film on a high mis-cut SrTiO_3 (111) substrate that can benefit from controllable surface termination through chemical etching [21]. The applicability of similar substrates to the epitaxial growth of Pd-, Pt-based metallic delafossites should be further studied. In addition, as mentioned in Ref. [10] to decrease the overall defect densities a higher growth temperature might be beneficial, although it can also lead to the formation of Co_3O_4 due to PdO volatility. The PdCoO_2 film in this paper was measured to be stoichiometric by Rutherford backscattering spectrometry, having a Pd:Co ratio of 1:1 with an accuracy of $\pm 2\%$. Therefore, we can expect that if the film is slightly

more off-stoichiometric, the defect density would increase even further.

IV. CONCLUSIONS

In this paper, we have looked at bulk single crystals and a thin-film PdCoO₂ using aberration-corrected STEM to understand the types and structures of unintentional defects. We have only observed ribbonlike defects in single crystals which require further investigation to determine the atomic details of their structures. On the other hand, epitaxially grown thin-film PdCoO₂ shows a myriad of defects including twin domains, OPBs, and Pd-rich agglomerates. The high concentration of defects indicates that improvements in film quality can be expected. Specific strategies identified to reduce the concentrations of the defects seen include using a substrate with a better structural match as well as the insertion of a suitable delafossite buffer layer that can be grown at higher temperature than PdCoO₂ to reduce its defect density before transitioning to PdCoO₂, which can only be grown at relatively low temperature by vacuum deposition methods. We hope our findings can lead to a deeper understanding of these fascinating materials whereas providing ideas to improve the growth of

thin films of PdCoO₂ and other delafossites for fundamental investigations as well as proof-of-principle device studies.

ACKNOWLEDGMENTS

This work was primarily supported by the U.S. Department of Energy, Office of Basic Sciences, Division of Materials Sciences and Engineering, under Award No. DE-SC0002334. Electron microscopy was performed in a facility supported by the National Science Foundation [Platform for the Accelerated Realization, Analysis, and Discovery of Interface Materials (PARADIM)] under Cooperative Agreement No. DMR-1539918. This work made use of the Cornell Center for Materials Research (CCMR) Shared Facilities, which are supported through the NSF MRSEC Program No. DMR-1719875. This work made use of a Helios FIB supported by NSF (Grant No. DMR-1539918) and the Cornell Center for Materials Research (CCMR) Shared Facilities, which are supported through the NSF MRSEC Program (Grant No. DMR-1719875). The FEI Titan Themis 300 was acquired through Grant No. NSF-MRI-1429155 with additional support from Cornell University, the Weill Institute, and the Kavli Institute at Cornell.

-
- [1] C. W. Hicks, A. S. Gibbs, A. P. Mackenzie, H. Takatsu, Y. Maeno, and E. A. Yelland, *Phys. Rev. Lett.* **109**, 116401 (2012).
- [2] V. Sunko, P. H. McGuinness, C. S. Chang, E. Zhakina, S. Khim, C. E. Dreyer, M. Konczykowski, H. Borrmann, P. J. W. Moll, M. König, D. A. Muller, and A. P. Mackenzie, *Phys. Rev. X* **10**, 021018 (2020).
- [3] A. P. Mackenzie, *Rep. Prog. Phys.* **80**, 032501 (2017).
- [4] C. Putzke, M. D. Bachmann, P. McGuinness, E. Zhakina, V. Sunko, M. Konczykowski, T. Oka, R. Moessner, A. Stern, M. König, S. Khim, A. P. Mackenzie, and P. J. W. Moll, *Science* **368**, 1234 (2020).
- [5] T. Harada, P. Bredol, H. Inoue, S. Ito, J. Mannhart, and A. Tsukazaki, *Phys. Rev. B* **103**, 045123 (2021).
- [6] T. Harada, K. Sugawara, K. Fujiwara, M. Kitamura, S. Ito, T. Nojima, K. Horiba, H. Kumigashira, T. Takahashi, T. Sato, and A. Tsukazaki, *Phys. Rev. Research* **2**, 013282 (2020).
- [7] P. Yordanov, W. Sigle, P. Kaya, M. E. Gruner, R. Pentcheva, B. Keimer, and H.-U. Habermeier, *Phys. Rev. Materials* **3**, 085403 (2019).
- [8] P. Yordanov, A. S. Gibbs, P. Kaya, S. Bette, W. Xie, X. Xiao, A. Weidenkaff, H. Takagi, and B. Keimer, *Phys. Rev. Materials* **5**, 015404 (2021).
- [9] T. Harada, K. Fujiwara, and A. Tsukazaki, *APL Mater.* **6**, 046107 (2018).
- [10] J. Sun, M. R. Barone, C. S. Chang, M. E. Holtz, H. Paik, J. Schubert, D. A. Muller, and D. G. Schlom, *APL Mater.* **7**, 121112 (2019).
- [11] M. Brahlek, G. Rimal, J. M. Ok, D. Mukherjee, A. R. Mazza, Q. Lu, H. N. Lee, T. Z. Ward, R. R. Unocic, G. Eres, and S. Oh, *Phys. Rev. Materials* **3**, 093401 (2019).
- [12] T. Harada, S. Ito, and A. Tsukazaki, *Sci. Adv.* **5**, eaax5733 (2019).
- [13] X. J. Wang, I. A. Buyanova, W. M. Chen, C. J. Pan, and C. W. Tu, *J. Appl. Phys.* **103**, 023712 (2008).
- [14] C. M. Brooks, R. B. Wilson, A. Schafer, J. A. Mundy, M. E. Holtz, D. A. Muller, J. Schubert, D. G. Cahill, and D. G. Schlom, *Appl. Phys. Lett.* **107**, 051902 (2015).
- [15] V. Eyert, R. Fresard, and A. Maignan, *Chem. Mater.* **20**, 2370 (2008).
- [16] K. P. Ong, J. Zhang, J. S. Tse, and P. Wu, *Phys. Rev. B* **81**, 115120 (2010).
- [17] See Supplemental Material at <http://link.aps.org/supplemental/10.1103/PhysRevMaterials.6.093401> for more information on the HAADF-STEM detection limit on point defects, the raw ABF-STEM image of Fig. 2(b), the schematics for energetically favorable Pd interstitial position, the raw ABF-STEM images, and the schematics for Fig. 4(a).
- [18] J. M. Johnson, S. Im, W. Windl, and J. Hwang, *Ultramicroscopy* **172**, 17 (2016).
- [19] D. G. Schlom, L.-Q. Chen, X. Pan, A. Schmehl, and M. A. Zurbuchen, *J. Am. Ceram. Soc.* **91**, 2429 (2008).
- [20] T. Sun, B. Yao, A. P. Warren, K. Barmak, M. F. Toney, R. E. Peale, and K. R. Coffey, *Phys. Rev. B* **81**, 155454 (2010).
- [21] J. M. Ok, S. Yoon, A. R. Lupini, P. Ganesh, A. Huon, M. F. Chisholm, and H. N. Lee, *ACS Appl. Mater. Interfaces* **13**, 22059 (2021).
- [22] M. Zurbuchen, W. Tian, X. Pan, D. Fong, S. Streiffer, M. Hawley, J. Lettieri, Y. Jia, G. Asayama, S. Fulk *et al.*, *J. Mater. Res.* **22**, 1439 (2007).
- [23] U. Kaiser, D. A. Muller, J. L. Grazul, A. Chuvulin, M. Kawasaki, A. Chuvilin, and M. Kawasaki, *Nature Mater.* **1**, 102 (2002).

- [24] J. M. Ok, M. Brahlek, W. S. Choi, K. M. Roccapiore, M. F. Chisholm, S. Kim, C. Sohn, E. Skoropata, S. Yoon, J. S. Kim, and H. N. Lee, [APL Mater.](#) **8**, 051104 (2020).
- [25] J. M. Ok, S. Yoon, A. R. Lupini, P. Ganesh, M. F. Chisholm, and H. N. Lee, [Sci. Rep.](#) **10**, 11375 (2020).
- [26] N. Wolff, T. Schwaigert, D. Siche, D. G. Schlom, and D. Klimm, [J. Cryst. Growth](#) **532**, 125426 (2020).